ELSEVIER

Dynamic imaging with MRI contrast agents: quantitative considerations

Mikhail G. Shapiro[a], Tatjana Atanasijevic[b], Henryk Faas[c], Gil G. Westmeyer[d], Alan Jasanoff[b,c,d,*]

[a]*Division of Biological Engineering, Massachusetts Institute of Technology, Cambridge, MA 02139, USA*
[b]*Department of Nuclear Science and Engineering, Massachusetts Institute of Technology, Cambridge, MA 02139, USA*
[c]*Department of Brain and Cognitive Sciences, Massachusetts Institute of Technology, Cambridge, MA 02139, USA*
[d]*Francis Bitter Magnet Laboratory, Massachusetts Institute of Technology, Cambridge, MA 02139, USA*

Abstract

Time-resolved MRI has had enormous impact in cognitive science and may become a significant tool in basic biological research with the application of new molecular imaging agents. In this paper, we examine the temporal characteristics of MRI contrast agents that could be used in dynamic studies. We consider "smart" T1 contrast agents, T2 agents based on reversible aggregation of superparamagnetic nanoparticles and sensors that produce changes in saturation transfer effects (chemical exchange saturation transfer, CEST). We discuss response properties of several agents with reference to available experimental data, and we develop a new theoretical model that predicts the response rates and relaxivity changes of aggregation-based sensors. We also perform calculations to define the extent to which constraints on temporal resolution are imposed by the imaging methods themselves. Our analysis confirms that some small T1 agents may be compatible with MRI temporal resolution on the order of 100 ms. Nanoparticle aggregation T2 sensors are applicable at much lower concentrations, but are likely to respond on a single second or slower timescale. CEST agents work at high concentrations and temporal resolutions of 1–10 s, limited by a requirement for long presaturation periods in the MRI pulse sequence.
© 2006 Elsevier Inc. All rights reserved.

Keywords: Contrast agent; Molecular imaging; Sensor; Temporal resolution; Superparamagnetic nanoparticle

1. Introduction

Many of life's most important processes occur within a fraction of a second. With temporal and spatial resolution orders of magnitude cruder than optical imaging, MRI seems a deeply insufficient tool for investigation of this "short-timescale physiology." But with opaque specimens, noninvasive imaging with MRI may still be a uniquely valuable approach. Echo planar pulse sequences allow images to be collected in tens of milliseconds — fast enough to freeze-frame the beating heart or record rapid fluctuations of blood flow in the brain [1]. In many other contexts, the limitation on MRI has not been its intrinsic acquisition rate, but rather the absence of contrast mechanisms that can translate biological events of interest into MRI-detectable signal changes.

Newly developed contrast agents, products of the growing field of molecular imaging, are beginning to change this situation [2,3]. Several groups have introduced agents useful for mapping static or slowly varying patterns of gene expression and epitope distribution [4–7]. Contrast agents have also been developed for sensing more dynamic variables such as pH [8–10], oxygen tension (pO_2) [11,12], ion and metabolite concentrations [13–15], and enzyme-catalyzed reactions [5,16]. These agents have been referred to as "smart" contrast agents and function as sensors in MRI, analogous to fluorescent probes used in optical imaging and microscopy. Some MRI sensors could, in principle, be applied to study fast (generally cellular) physiological events, for example: endocytic pH changes during vesicle recycling on the 1-s timescale, calcium signaling transients lasting 10–100 ms, pO_2 fluctuations within 2 s of modulations to oxidative metabolism and changes in protein phosphorylation in seconds to minutes during neuronal synaptic plasticity. In each case, however, the practical time resolution attainable with contrast agent-enhanced MRI may be limited by the agent's molecular properties and by the physical requirements of contrast generation.

* Corresponding author. Department of Nuclear Science and Engineering, Massachusetts Institute of Technology, Cambridge, MA 02139, USA. Tel.: +1 617 452 2538; fax: +1 617 253 0760.
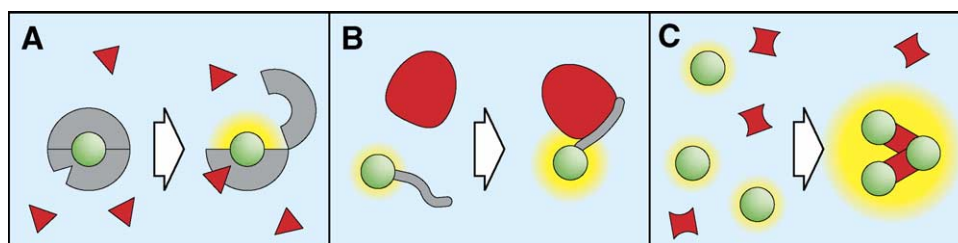*E-mail address:* jasanoff@mit.edu (A. Jasanoff).

Fig. 1. Smart contrast agent mechanisms. Contrast agents have been constructed to respond to physiological targets by a variety of mechanisms. In (A), binding of a target molecule (red) to a paramagnetic chelate (green and gray) increases exposure of the agent's coordinated metal ion (green, usually Gd) to surrounding tissue water (blue), allowing water molecules to participate in inner sphere interactions with the metal and increasing the agent's T1 relaxivity. Enzyme and ion-sensitive contrast agents that work this way have been synthesized. (B) Association of a lanthanide chelate (green and gray) with a much larger binding partner (red) results in an increase in rotational correlation time (τ_R) and T1 relaxivity. (C) The presence of a target molecule (red) induces aggregation of functionalized superparamagnetic nanoparticles (green). Aggregation can induce dramatic changes in T2.

Characteristics of contrast agents and methods for their detection vary widely. Historically, the most commonly used are small paramagnetic metal chelates which act by shortening T1 (longitudinal) relaxation times [17]. MRI sensors (Fig. 1) have been constructed from these agents by coupling determinants of their T1 relaxivity—solvent accessibility, rotational correlation time, or the spin and redox state of the metal—to the presence of specific molecular targets. Sensors based on T2 (transverse) relaxation rate changes have also been produced, most recently by coupling the aggregation state of superparamagnetic iron oxide nanoparticles (SPIOs) to physiological signals of interest. Aggregation of SPIOs even in concentrations as low as 10 mg/L can change observed T2s quite dramatically [18]. A third family of MRI sensors has been based on chemical exchange saturation transfer (CEST) effects [19]. Labile protons or water molecules bound to a CEST agent can be selectively saturated and will exchange with bulk solvent protons to decrease the local MRI signal. In CEST-based sensors, the exchange rate or chemical shift of bound protons is modulated by interaction with the sensor's target [20,21].

To be useful for dynamic imaging studies, an MRI sensor must produce a fast and large enough signal change to be detected on the desired timescale. Although the steady-state detection thresholds for various contrast agents have been discussed extensively in the literature (e.g., Refs. [22–25]), the interaction between sensitivity and dynamics has been less thoroughly examined. At the same time, a systematic analysis of advantages and disadvantages of available contrast mechanisms is essential to the development of effective strategies for fast-timescale molecular imaging. In this paper, we review the molecular mechanisms of some paradigmatic smart T1-, T2- and CEST-based contrast agents, and consider the agents' response rates using a combination of simulations and reference to existing experimental data. Throughout the paper, we estimate the temporal resolution of each molecular imaging strategy as the inverse of the duration of the impulse response that relates an underlying stimulus or change in conditions, via the contrast agent and MRI pulse sequence, to a detectable signal change. Because of the importance of the MRI acquisition method in determining this temporal resolution, we include a discussion of detection methods themselves along with consideration of the different classes of molecular imaging agents.

2. Materials and methods

2.1. Bloch equation simulations

Magnetization trajectories were estimated by using Euler integration of the Bloch equations to simulate one or two spin-pool evolution in the presence of relaxation and chemical exchange. Radiofrequency (RF) excitation pulses were modeled as instantaneous rotations, and Larmor precession was omitted from the calculations. Presaturation used in CEST simulations was modeled as a π pulse train delivered at a fixed frequency (generally 2 kHz) during a presaturation period TP. Parameter settings are noted where appropriate in the text. Time steps used in the calculations were chosen to be a factor of 10 below the smallest characteristic time relevant to the simulation. Macroscopic susceptibility effects (i.e., T2* relaxation components) were omitted. All simulations were performed using custom routines running under Matlab (Mathworks, Natick, MA, USA) on a Linux-based workstation.

2.2. SPIO aggregation simulations

SPIO aggregation and disaggregation were simulated using the Euler method, applied to the Smoluchowski equation [see Eq. (16) below], which describes the transition rates among single particles and aggregates of all allowable sizes. The aggregation kernel K_{agg}, adapted from Odriozola et al. [26], describes the rate constant for binding of two aggregates of compositions (i, j) and (k, m) as a function of their diffusion-limited collision rate and their probability of sticking upon collision:

$$K_{agg}(i,j,k,m) = k_{dl}(i,j,k,m)$$
$$\times \frac{P_{stick}(i,j,k,m)\varepsilon[(i+j)(k+m)]^b}{1 + P_{stick}(i,j,k,m)\left\{\varepsilon[(i+j)(k+m)]^b - 1\right\}} \quad (1)$$

where ε and b correspond to Odriozola's constants N_{11} and b, respectively, with respective values of 6.1 and 0.35. $k_{dl}(i, j, k, m)$ is the diffusion-limited collision rate due to Brownian motion, given by:

$$k_{dl}(i,j,k,m) = \frac{2k_B T}{3\eta}\left([i+j]^{1/df} + [k+m]^{1/df}\right)\left([i+j]^{-1/df} + [k+m]^{-1/df}\right)$$

(2)

where k_B is the Boltzmann constant, T is the absolute temperature, η is the medium viscosity and df is the fractal dimension of the aggregates (assumed to be constant throughout aggregation). $P_{stick}(i, j, k, m)$ is the sticking probability of the two aggregates, given by:

$$P_{stick}(i,j,k,m) = P_{11}\left[N_i\left(\frac{i}{i+j}\right)N_m\left(\frac{m}{m+k}\right) + N_k\left(\frac{k}{k+m}\right)N_j\left(\frac{j}{i+j}\right)\right]$$

(3)

where N_x for $x=i,j,k,m$ represents the fraction of functional groups of the corresponding type available for binding, e.g.:

$$N_i = \frac{(f-1)i - j + 1}{fi}$$

(4)

where f is the number of functional groups per particle and (i, j) is the aggregate composition. P_{11} is the sticking probability for a collision of two oppositely functionalized monomers, which we estimated by assuming cubical geometry for the two types of functional groups, with sides of length d_a and d_b, and calculating the fraction of the particle surface that is covered by the functional group (for given functionalization ratios f and g and particle radius r). The product of these surface fractions is then multiplied by the bimolecular sticking probability P_{bm} for free functional groups in solution, which may be roughly estimated as the ratio of their known binding on-rate k_{on} and their theoretical diffusion-limited collision rate. We include an additional factor of 6 to account for an assumption that the cubic functional groups are optimally oriented on the particle surface. The resulting expression is:

$$P_{11} = P_{bm}\left(\frac{6fd_a^2}{4\pi r^2}\right)\left(\frac{6gd_b^2}{4\pi r^2}\right)$$

(5)

The fragmentation kernel K_{frag}, adapted from Laurenzi and Diamond [27], describes the rate constant of fragmentation of an aggregate of composition $(i+k, j+m)$ into two aggregates (i, j) and (k, m):

$$K_{frag}(i,j,k,m) = k_{off}\left[A_f(i,j)A_g(k,m) + A_f(k,m)A_g(i,j)\right]$$
$$\times \frac{N_{iso}(i,j)N_{iso}(k,m)}{N_{iso}(i+k,j+m)}$$

(6)

Here, k_{off} is the bimolecular dissociation rate for the complimentary functional groups. A_f and A_g are the number of free functional groups of the two types in aggregates of a given composition, i.e.:

$$A_f(i,j) = (f-1)i - j + 1; \quad A_g(i,j) = (g-1)j - i + 1$$

(7)

N_{iso} is a combinatorial factor describing the number of possible arrangements of particles in an aggregate of a given composition:

$$N_{iso}(i,j) = \frac{f^i g^j (fi-i)!(gj-j)!}{\left[A_f(i,j)\right]\left[A_g(i,j)\right]i!j!}$$

(8)

In order to minimize the computational cost of our simulation, we imposed an upper limit on the allowed aggregate size, $C(z, z)$, with $z=45$. This limit allowed the kernels to be predefined, greatly speeding up the simulations. Under simulation conditions that favor extensive aggregation, this limit causes an underestimation of average particle size and an accumulation, or "bunching", of the aggregate population at sizes near the maximum. However, the parameters used in most of our runs produced aggregates with average sizes well below this upper limit and resulting size distributions that did not exhibit significant bunching. When noticeable bunching did occur, it produced only a minimal effect on simulation time courses (below 5% for T_{obs}), with "saturating" effects on steady-state size evident only when this size approached $2z$.

Unless otherwise noted in the main text, the parameters used in our aggregation simulations were as follows: $k_{on}=10^6\,M^{-1}\,s^{-1}$, $k_{off}=6\times10^{-4}\,s^{-1}$, $f=50$, $g=50$, $r=15$ nm, df=2.2, $T=300$ K, $\eta=1$ cp, R2 (nonaggregated relaxivity)=20 $(mM\ Fe)^{-1}\,s^{-1}$, Fe atoms per particle=2064. The same equations and parameters were used to simulate disaggregation, but with a factor of 10^2 decrease in k_{on} and a factor of 10^2 increase in k_{off}.

2.2.1. Additional calculations and data presentation

Additional computations, including calculations of percent signal change for T1 and CEST imaging, were performed using Matlab. Kaleidagraph (Synergy Software, Reading, PA, USA) and Adobe Illustrator (Adobe Systems, San Jose, CA, USA) were used in the preparation of figures.

3. Results and discussion

3.1. Dynamic imaging with smart T1 contrast agents

3.1.1. Temporal resolution of T1-weighted imaging

Several of the first MRI sensors were T1 agents synthesized by Meade and colleagues, which respond to their targets with roughly twofold changes in T1 relaxivity [5]. Changes in T1 induced by these agents are usually detected using gradient-recalled echo (GRE), spin-echo (SE) or inversion-recovery (IR) imaging pulse sequences [28]. The T1 observed in the presence of a smart T1 contrast agent is given by the approximation, generally valid for low agent concentrations ([M]):

$$\frac{1}{T1(t)} = \frac{1}{T1_0} + R1(t)[M]$$

(9)

where $T1_0$ is the background T1 in the absence of contrast agent and $R1(t)$ is the time-dependent relaxivity of the
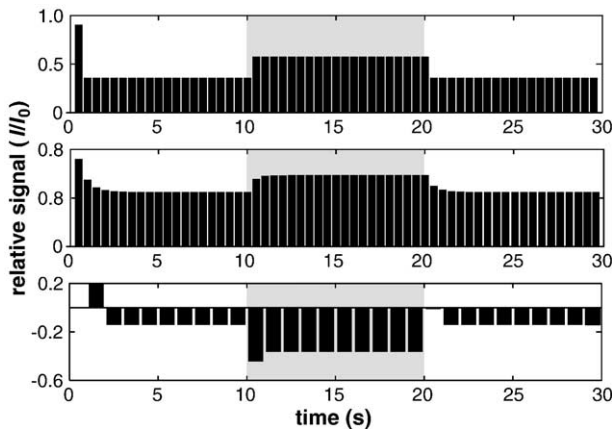
Fig. 2. Effect of excitation flip angle on T1 image series. Magnetization trajectories during T1-weighted MRI time series were simulated using the Bloch equations. To model the effect of a smart T1 agent, the T1 of the system was set to a baseline of 1.0 s, but reduced by a factor of two during a 10-s "stimulus" period (gray boxes). The top two panels show results from a mock gradient echo (GRE) imaging sequence with 0.5 s TR, 10 ms TE and 100 ms T2, beginning with longitudinal magnetization at equilibrium (=1.0). The top panel shows the echo peak signal series obtained when perfect $\pi/2$ pulses are used for excitation: a transition in signal level takes place sharply after the change in T1. The middle panel shows the effect of Ernst angle excitation. Although the overall signal level is higher, the increase in signal after T1 decreases is slower. In the bottom panel, an inversion-recovery sequence is simulated with a 0.5-s recovery time and 1.0 s TR. As with Ernst angle GRE imaging, the signal at each acquisition is dependent on the previous acquisition, and the new equilibrium signal is reached only after two or more acquisitions after a change in T1.

contrast agent; R1(t) could also be rewritten as R1$_0$+ΔR1(t), where R1$_0$ is the "resting" relaxivity and ΔR1(t) is the temporally varying component of relaxivity, typically linked to a phenomenon of interest.

The sampling rate of a time varying T1-weighted signal is determined by 1/TR, where TR is the repetition time of the pulse sequence; entire three-dimensional volumes may be acquired with each repetition if echo planar readout (EPI) is used. The contrast-to-noise ratio (CNR) of a GRE or SE imaging method designed to detect changes in T1 is maximized when TR equals <T1(t)>, the average value of T1 over time, and when Ernst angle RF excitation is used [in a GRE pulse sequence, this means that the flip angle α would be set equal to $\cos^{-1}(\exp\{-TR/T1\})$]. In contrast, the temporal resolution of a T1-weighting scheme is maximized when the RF flip angle is set to $\pi/2$ — only under this condition is the signal observed at each time point independent of the T1 observed in the previous acquisition. For the same reason, GRE or SE imaging with $\pi/2$ excitation achieves better temporal resolution than IR imaging, despite the advantages of IR for measurements of absolute T1. Fig. 2 demonstrates these effects in simulated T1-weighted signals acquired with $\pi/2$ and Ernst angle GRE, and with standard IR pulse sequences. Practical consequences of the sensitivity of dynamic T1-weighted imaging to flip angle are that SNR sacrifices may be required to optimize temporal resolution, particularly for

short TR values, and that spatially varying RF excitation (e.g., produced by a surface coil) is likely to produce inhomogeneous temporal dependence.

With T1-weighted GRE or SE acquisition (echo time $\ll$ T2, TR) and ideal $\pi/2$ pulse excitation, the relative signal (I_n) at the end of the nth acquisition period is given by:

$$I_n \propto 1 - \exp\left\{ -\int_{t_{n-1}}^{t_{n-1}+\mathrm{TR}} \frac{1}{\mathrm{T1}(t)} dt \right\} \qquad (10)$$

where t_{n-1} and t_n ($=t_{n-1}+$TR) are the RF excitation times preceding the ($n-1$)th and nth acquisitions, respectively. The recorded T1-weighted MRI signal therefore reflects the history of T1 between each RF excitation and the next, so contributions from instantaneous events cannot be recognized with temporal resolution better than that defined by TR. Assuming ideal flip angles are used, the time resolution of a T1-weighted molecular imaging experiment will therefore be limited by the smallest TR consistent acceptable MRI contrast changes given the amount of T1 change produced by the contrast agent and the noise level of the scanner.

3.1.2. Response rates of T1-based MRI sensors

T1 contrast agents are typically organic complexes containing a paramagnetic metal ion such as gadolinium (Gd), which strongly promote the relaxation of the water protons due to the influence of unpaired electron spins of the metal ion. Factors that are important in determining the relaxivity of a contrast agent (reviewed in Refs. [17,29]) are contained in the Solomon–Bloembergen–Morgan (SBM) equations; these include timescales for various molecular motions, structural features of the contrast agent and spin properties of the paramagnetic metal ion. Some of these properties can be manipulated in such a way as to produce a change in relaxivity coupled to specific events. Among them are the coordination number of the water molecules, q; the lifetime of the water molecule in the complex, τ_m; and the rotational correlation time of the whole complex, τ_R. If one of these parameters differs significantly between two "states" or conformations of a contrast agent, the intensity of the signal observed with MRI is also changed. The timescale on which the change occurs is strongly dependent on the type of the contrast agent and on which property has been affected.

The best explored class of T1 contrast agents relies on the change in solvent exposure to the paramagnetic metal ion (Fig. 1A) [30]. The resting state of the contrast agent usually has relatively low relaxivity, with limited water access to the metal ion. The contrast agent is switched into a state of higher relaxivity by a biochemical trigger, such as the activity of an enzyme or a spike in concentration of an intracellular messenger. Several agents that work by this type of mechanism have been reported in the literature. Louie et al. [5] synthesized a caged contrast agent called EgadMe, which is a substrate for the enzyme

β-galactosidase. The activity of β-galactosidase uncages the agent by cleaving a galactopyranosyl group, exposing a Gd coordination site to raise the agent's effective q from 0.65 to 1.02; this structural change in turn gives rise to an increase in T1 relaxivity from 0.903 to 2.72 mM^{-1} s^{-1} (measured at 11.7 T). Like many enzymes, β-galactosidase obeys so-called Michaelis–Menten kinetics, meaning that the rate of product formation depends on parameters k_{cat} and K_m in the following equation:

$$V = \frac{k_{cat}[E]_0[S]}{K_m + [S]} \qquad (11)$$

where $[E]_0$ is the total enzyme concentration, $[S]$ is the substrate (caged contrast agent) concentration and V is the rate of uncaged product formation in moles per second. The cleavage of EgadMe takes place with a k_{cat} of 2.4×10^{-3} nmol U^{-1} s^{-1} and a K_m of 0.0182 mM; this means for example that a 100-µM concentration of the agent would require on the order of several minutes to be cleaved by 100 U/ml (~1 µM) of β-galactosidase. Enzymes most likely to be useful for activating contrast agents are those that cleave carbon–carbon, carbon–nitrogen or carbon–oxygen bonds; these typically have a k_{cat} significantly smaller than 1 s^{-1} and are therefore likely to process their substrates over timescales much longer than the TR of a typical T1-weighted imaging sequence. In these cases, the temporal resolution of the method would be limited by the enzyme activity level, although with large enough enzyme and substrate concentrations the onset of enzyme activity might be recognized with TR-limited precision.

Faster relaxivity changes are likely to be produced by ion-sensing MRI contrast agents. Sensors for calcium and for zinc have been produced [13,14]; as with EgadMe, they respond to their targets with conformational changes that expose a bound gadolinium atom to water. T1 relaxivity changes from 3.26 to 5.76 mM^{-1} s^{-1} (11.7 T), and from 4 to 6 mM^{-1} s^{-1} (7 T), for the calcium and zinc sensors, respectively. No kinetic data are available for either of these contrast agents, but because their mechanisms are somewhat similar to small fluorescent ion sensors, the response rates of these sensors may be relevant. In particular, the calcium-sensitive agent synthesized by Li et al. [13] has similar affinity and calcium-liganding groups to Fura-2 and related BAPTA-based "fast" calcium sensors. These dyes have measured k_{on} for calcium on the order of 10^9 M^{-1} s^{-1} [31]. Assuming an MRI calcium sensor had an equivalent k_{on} and a K_d of 1 µM, and if it was used at a concentration of 100 µM to detect (buffered) calcium concentration fluctuations between 0.1 and 2 µM, its overall response rate would be limited by dissociation and would likely be close to a millisecond. This rate is two orders of magnitude below practical TR values. Time resolution in imaging experiments using MRI ion sensors would therefore be determined by the repetition rate of the imaging procedure.

Another method shown to enhance the relaxivity of a T1 contrast agent is to increase its rotational correlation time, τ_R. For small molecules, τ_R dominates the total correlation time (τ_C), a parameter that enters into the SBM equations and strongly influences the magnetic field dependence of T1 relaxivity. Since

$$\tau_R = 4\pi a^3 \eta / 3 k_B T \qquad (12)$$

where k_B is the Boltzmann constant; changes in τ_R could be effected either by manipulating the viscosity (η) or temperature (T) of the system, or by changing the effective radius (a) of the contrast agent. MRI contrast changes due to changes in the τ_R of a T1 agent are sometimes dramatic, and sensors involving changes in τ_R (Fig. 1B) may be particularly valuable for dynamic imaging at today's most common clinical scanner field strengths (≤ 3 T).

De Leon-Rodriguez et al. [32] followed these principles and designed a paramagnetic peptide (Gd^{3+}-G80BP) that senses its protein target (Gal80) by binding to it; a related, but enzyme-dependent approach was taken in a study by Aime et al. [11]. In the Gal80/Gd^{3+}-G80BP case, association produces a roughly 25-fold increase in τ_R, corresponding to the ratio of Gal80 complex to free peptide molecular sizes (here assuming equal density). At 0.5 T, the binding reaction produced a T1 relaxivity change from 8.3 to 44.8 mM^{-1} s^{-1}. Protein–protein association rates tend to be on the order of 10^6 M^{-1} s^{-1} [33,34], meaning that a high-affinity binding reaction initiated by 10 µM concentrations of dissociated species might approach its equilibrium with a characteristic time on the order of 0.1–1 s. Dissociation rates for this type of interaction vary widely, but will be slower for complexes with $K_d \ll 10^{-5}$. Because these timescales are on the order of typical T1-weighted MRI TR values, sensors based on protein binding-induced changes in τ_R may often, but not always, respond with rates that are limiting for the temporal resolution of a dynamic MRI experiment.

3.2. Dynamic imaging with SPIO aggregation-based T2 agents

3.2.1. Temporal resolution of T2-weighted imaging

An endogenous T2 contrast agent (deoxyhemoglobin) and an exogenous blood-pool contrast agent (mononuclear SPIO or MION) have been heavily used in dynamic functional brain imaging experiments (fMRI), where contrast and temporal resolution are governed by hemodynamic effects [35,36]. Smart iron oxide agents have also been introduced and applied in cell labeling, cell tracking and molecular sensing [18,37]. Although they are physically large (10–100 nm), an advantage of SPIO agents is that they have high relaxivities (10–100 mM^{-1} Fe s^{-1}) and are detectable at very low particle concentrations — several orders of magnitude below concentrations required for most T1 agents [38,39]. SPIO agents also produce magnetic susceptibility variations that may be visualized even at fairly low spatial resolution by T2*-weighted imaging.

T2-weighted imaging is usually performed using SE pulse sequences, sometimes in conjunction with Carr–Purcell–Meiboom–Gill (CPMG) readout [28]. GRE sequences can be used to produce related T2*-weighted images. Contrast is established during the echo time (TE) of these sequences or across multiple echo times with CPMG. Assuming T1 and TR are static or that TR $\gg$ T1, the relative T2-weighted signal in a single-echo (GRE) sequence is given by:

$$I_n \alpha \exp\left\{ - \int_{t_n}^{t_n+\text{TE}} \frac{1}{\text{T2}(t)} dt \right\} \tag{13}$$

where T2 is affected by the T2 contrast agent's relaxivity (R2) according to:

$$\frac{1}{\text{T2}(t)} = \frac{1}{\text{T2}_0} + [\text{R2}_0 + \Delta\text{R2}(t)][\text{M}] \tag{14}$$

where T2_0 is the background T2, and R2_0 and $\Delta\text{R2}(t)$ are the static and time-dependent components of T2 relaxivity, respectively. Because echo times are usually short (10–100 ms), and necessarily less than TR, the temporal "precision" of T2-weighted imaging can be considered to be higher than that of T1-weighted imaging. On the other hand, unless CPMG or phase-locking strategies are used, the image sampling rate is still limited by TR, and very short T2 changes may be missed entirely with probability $(1-\text{TE/TR})$, even if they would be likely to produce a signal change when sampled optimally. A clear advantage of scan series data obtained with T2-weighted imaging sequences, however, is that their time dependence does not depend on the RF flip angle.
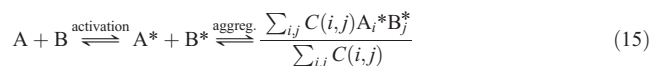
3.2.2. SPIO aggregation sensors

Several types of T2 relaxation-promoting smart contrast agents have been produced. Of these, agents based on the aggregation of biocompatible SPIO nanoparticles demonstrate the largest relaxivity changes and appear to be easily tailored to a variety of applications [18]. Superparamagnetic sensors are formed by functionalizing the surfaces of SPIOs with molecules (usually biomolecules, i.e., proteins or nucleic acids) that associate with complementary groups on other SPIOs, either when activated in some way or when bridged by a particular target molecule of interest. Because the particles are multivalent, this binding or bridging induces formation of aggregates, somewhat similar to the process of immunoprecipitation. Aggregation can dramatically amplify the transverse relaxivity of SPIOs, significantly reducing the T2 relaxivity even of very dilute SPIO suspensions (<10 mg/L Fe). Perez et al. [16,40,41] pioneered this approach and have applied it to make MRI sensors for specific oligonucleotides, protease and nuclease activity, and protein–protein binding, including antibody/epitope recognition. Our group has adapted this approach to construct an SPIO bioconjugate sensor for calcium [42].

The strong T2 effects produced by SPIO sensors make these contrast agents potentially attractive tools for dynamic MRI studies in vivo. Little is currently known, however, about the response dynamics of aggregation-based sensors. Most of the existing SPIO sensors appear to respond to their targets on a several-minute timescale, although some enzyme-dependent variants are slower. It is currently unknown to what extent design characteristics of the sensors affect rates of aggregation and concomitant relaxivity changes. Given the relative absence of experimental data related to biofunctionalized nanoparticle aggregation kinetics, we here explore theoretical determinants of SPIO aggregation dynamics in some detail through computational modeling, with the goal of identifying key parameters affecting the time courses and extents of aggregate formation. In addition, we apply a rudimentary approach to approximating changes in T2 relaxivity produced by SPIO aggregates; this allows us to convert calculated aggregation times into estimated MRI signal changes.

3.2.3. Model of SPIO aggregation behavior

To model physiologically induced SPIO aggregation dynamics, we considered the following reaction scheme:

$$\text{A} + \text{B} \underset{}{\overset{\text{activation}}{\rightleftharpoons}} \text{A}^* + \text{B}^* \overset{\text{aggreg.}}{\rightleftharpoons} \frac{\sum_{i,j} C(i,j)\text{A}_i^*\text{B}_j^*}{\sum_{i,j} C(i,j)} \tag{15}$$

where A and B denote two types of bioconjugated SPIO nanoparticles with different functional groups. Under resting or baseline conditions, the groups on A and B particles have minimal binding affinity for one another. When one or both of the two types of functional groups are activated (converting A to A* and B to B*), their binding affinity increases, initiating the process of particle aggregation. The end-product of the aggregation is a distribution of clusters [denoted by the summation ratio on the right-hand side of Eq. (15)] with compositions A_i^*B_j^* and concentrations $C(i, j)$, where i is the number of A-type particles and j is the number of B-type particles in a given aggregate of total size $i+j$. Disaggregation can be induced by deactivating the functional groups, causing dissociation at the molecular level; here we assume that dissociation need not precede deactivation. For simplicity, we also assume that the activation and deactivation steps happen much faster than aggregation and disaggregation. In many cases, this is a reasonable approximation, given the relatively slow timescales for aggregate (dis)assembly (1–1000 s) compared to the timescales of potential (de)activation events (e.g., milliseconds for Ca^{2+}-induced protein conformational changes). Some triggering events, like enzymatic proteolysis, might be much slower, however, in which case the fast-activation condition would be violated and the model we develop would have to be modified.

Aggregation phenomena are commonly formulated using the Smoluchowski equation [43], a general differential equation describing the formation and fragmentation of various size aggregates. The Smoluchowski model assumes
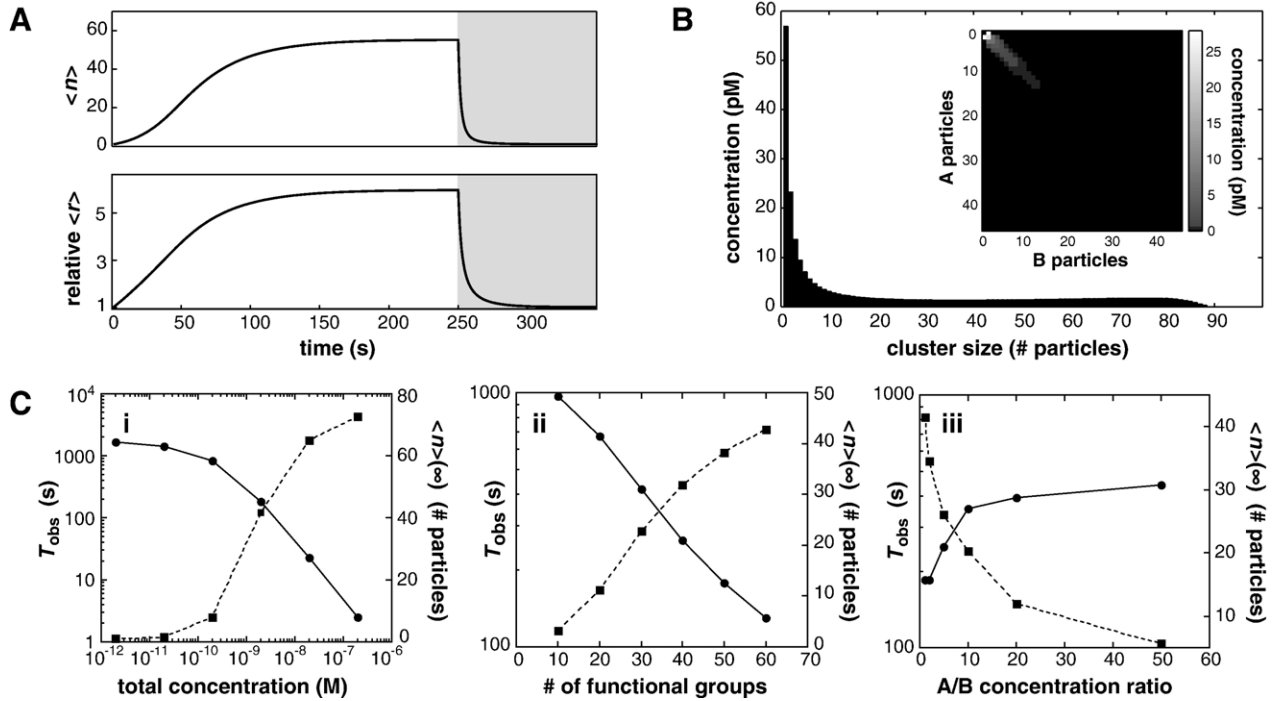
Fig. 3. Predicted characteristics of nanoparticle aggregation and disaggregation. (A) The temporal evolution of mass-weighted average aggregate size $<n>(t)$ (top) and radius of gyration relative to monomer (bottom) during aggregation and disaggregation. (B) The steady-state aggregate size distribution corresponding to $t=250$ s in (A). The insert shows the composition distribution of the aggregates, with the number of type A and type B particles on the horizontal and vertical axes, respectively. (C) Apparent aggregation time constant T_{obs} (circles) and steady-state mass-weighted average aggregate size $<n>(\infty)$ (squares) for a range of initial monomer concentrations (i), functionalization densities (functional groups per particle) (ii) and concentration ratios between the complementary particle types (iii). Simulation parameters are listed in the Materials and methods section.

that every transition in the system involves either the break-up of an aggregate into two smaller species or the agglomeration of two aggregates into a larger cluster:

$$\frac{dC(u,v)}{dt} = \frac{1}{2}\sum_{i=0}^{u}\sum_{j=0}^{v}K_{agg}(i,j,u-i,v-j)C(i,j)C(u-i,v-j)$$
$$- \frac{1}{2}\sum_{i=0}^{u}\sum_{j=0}^{v}K_{frag}(i,j,u-i,v-j)C(u,v)$$
$$- \sum_{i=0}^{z-u}\sum_{j=0}^{z-v}K_{agg}(i,j,u,v)C(i,j)C(u,v)$$
$$+ \sum_{i=0}^{z-u}\sum_{j=0}^{z-v}K_{frag}(i,j,u,v)C(u+i,v+j)$$

(16)

Here, $C(u, v)$ is the concentration of aggregates that contain u particles of type A and v particles of type B. The coefficients K_{agg} and K_{frag} are "kernels" for aggregation and fragmentation, respectively — they function like rate constants and reflect the probability that aggregates of size (u, v) will be formed by or broken into clusters of all other allowed sizes. The first term of Eq. (16) is the instantaneous rate at which aggregates of composition (u, v) are formed through the binding of all possible pairs of smaller aggregates. Similarly, the second term accounts for the breakup of (u, v) clusters into all possible smaller fragment pairs. The third term is the rate at which aggregates of

composition (u, v) bind to other clusters. The final term is the rate at which (u, v) clusters break off from larger aggregates of size $(u+i, v+j)$. K_{agg} and K_{frag} were adapted from the literature [26,27] in order to reflect the scenario in Eq. (15). As is common in other models, our approach assumed that the aggregates are fractal (irregular at all length scales) and noncircular (any two particles are connected through only one chain). These assumptions are valid for rigid particles with small (protein-sized) functional groups tightly anchored to the particle surface. See Materials and Methods for further details.

In order to simulate the aggregation of SPIOs, we used Euler integration to obtain mass-action solutions to Eq. (16). Fig. 3A shows representative aggregation and disaggregation time courses produced by our simulations. We depict both the mass-averaged mean particle radius $<r>$ (relative to an individual particle) and the mass-averaged mean aggregate size $<n>$ as functions of time. The corresponding steady-state distribution (limit at infinite time) of aggregate sizes and compositions is shown in Fig. 3B. These time courses and distributions are consistent with results from previous Monte Carlo simulations and experiments involving general reversible aggregation phenomena [27,44]. To facilitate the comparison of time courses for varying sets of parameters, we defined an "apparent" aggregation time constant T_{obs} as the value for which $[<n>(T_{obs})-<n>(0)]$

equals $(1-1/e)[<n>(\infty)-<n>(0)]$, where $<n>(\infty)$ is the steady-state value of $<n>$ (as t goes to infinity), for an aggregation process initiated at $t=0$.

Our simulations investigated the dependence of T_{obs} and $<n>(\infty)$ on the total nanoparticle concentration, the number of functional groups per particle and the concentration ratio of complementary particles. The results, shown in Fig. 3C, demonstrate a generally nonlinear dependence of T_{obs} and $<n>(\infty)$ on these parameters. As concentration increases, both the rate of approach to equilibrium and the steady-state size rise in a supralinear fashion (panel C-i), as would be expected for a multibody process. For increasing number of functional groups per particle, T_{obs} approximates an inverse exponential dependence, while $<n>(\infty)$ increases roughly linearly (panel C-ii). As shown in panel C-iii, the maximal aggregation rate and size are found when the concentrations of complementary particles are equal. Overall, these results suggest that the kinetics of aggregation are highly sensitive to the particulars of their design and deployment, with aggregation times varying over three orders of magnitude within a feasible concentration and functionalization range. At the higher end of this range, theoretically achievable aggregation times are as short as several seconds.

As shown in the sample time courses of Fig. 3A (gray regions), disaggregation upon the removal of the activating physiological stimulus can occur on timescales considerably faster than those seen for aggregation. However, the rate of disaggregation can vary widely depending on the specific deactivation mechanism. For example, given an allosteric mechanism where activation and deactivation of particle functional group(s) can occur in both bound and unbound states, deactivation can be expected to increase dramatically the bimolecular dissociation rate k_{off} (in addition to reducing k_{on}), leading to fast disaggregation. By contrast, if the functional group(s) can only be deactivated in the unbound state, k_{off} remains unchanged for bound particles, resulting in a much slower disaggregation process. In general, at low nanoparticle concentrations, we expect disaggregation to occur faster than aggregation, making aggregation the limiting factor in the reversible response rate of an aggregation-based sensor.

It should also be noted that the rates of aggregation and disaggregation in biological tissues (e.g., cell cytoplasms) may be significantly slower than the rate observed in solution [45]. Experiments have shown that molecular crowding in the cellular milieu reduces the effective diffusivity of solutes in a size-dependent manner, decreasing it by roughly a factor of 4 for most biological molecules and by a factor of 40 or more for particles with diameters above a 50- to 80-nm threshold. Single SPIOs in the 30-nm size range should fall below this threshold, but aggregates larger than a certain size will be above it. Since under many conditions monomers are the single most common species in the aggregation reaction, it may be possible to roughly approximate the slowing of aggregation in the cellular environment by dividing the Brownian diffusivity constant by around a factor of 4 (here we assumed that diffusion of each aggregate was determined by the Stokes–Einstein equation only).

3.2.4. SPIO aggregation-induced changes in relaxivity

The model developed above makes predictions about the dependence of SPIO aggregation rate on various parameters of MRI sensors; aggregation time constants are likely to vary from several seconds to many minutes, depending on concentration, functionalization, monomer ratio and, in biological environments, size. But how is the aggregation rate of these particles likely to translate into MRI-observable signal changes? Although strong changes in T2 relaxivity upon aggregation of SPIOs have been reported, little work has been done to explain the mechanism of aggregation-induced contrast change. Previous theoretical analyses, Monte Carlo simulations and experimental work have shown that the T2 relaxivity of iron oxide nanoparticles is well described by the motional averaging approximation when mean Larmor frequency shift at the particle surface ($\Delta\omega$) and the time constant for water diffusion around the particle (τ_d) satisfy the condition $\tau_d\Delta\omega<1$ [46,47]. This condition is fulfilled for uncoated iron oxide crystals smaller than approximately 30 nm. For coated SPIOs such as MION-46 [48], which contains a crystalline core of around 5 nm diameter surrounded by an organic shell of roughly 10 nm thickness, this maximum size for motional averaging is relaxed to around 350 nm, due to a lower field strength at the particles' water-accessible outer surfaces.

In the motional averaging regime, outer sphere theory predicts the component of T2 relaxation due to a suspension of field-perturbing SPIO particles to be given by:

$$1/T2_{SPIO} = (4/9)V(\Delta\omega)^2\tau_d \tag{17}$$

where V is the volume fraction of solution occupied by the particles, τ_d is defined as $\tau_d=r^2/D$, where r is the particle radius and D is the self-diffusion coefficient of water, and $\Delta\omega$ is given by $\Delta\omega=(1/3)\mu_0\gamma M$, where M is the particle magnetization, μ_0 is the free space magnetic permeability and γ is the proton gyromagnetic ratio.

For aggregate sizes below the motional averaging cutoff, Eq. (17) and the definition of τ_d predict an increase in relaxivity proportional to the square of aggregate radius. For fractal aggregates, the relationship between the number of particles in the aggregate (n) and its radius of gyration (r) is:

$$r\propto n^{1/df} \tag{18}$$

where df is the aggregate's fractal dimension. Typically, df is between 1.75 and 2.3 in fractal aggregates [49,50], with reaction-limited aggregation (see above) resulting in larger df.

In addition, Eq. (17) and the definition of $\Delta\omega$ predict a quadratic dependence of relaxivity on particle magnetization, M. At field strengths above 1 T, SPIO magnetic moments are known to be saturated [48]. Under these
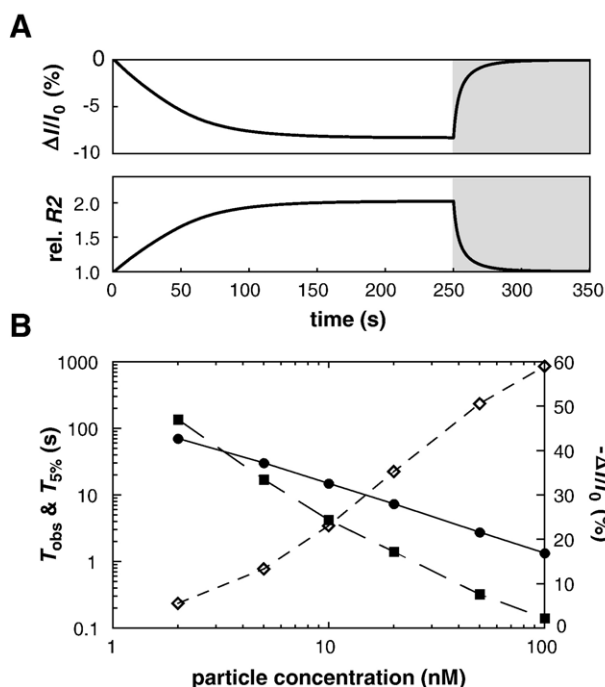
Fig. 4. Relaxivity changes during SPIO aggregation and disaggregation. (A) The temporal evolution of percent MRI signal change (top) and ratio of net T2 relaxivity, relative to unaggregated monomer solution (bottom), corresponding to the aggregation time course shown in Fig. 3A. (B) Apparent signal change time constant T_{obs} (filled circles), time to reach a 5% signal change $T_{5\%}$ (filled squares) and the steady-state percent signal decrease (hollow diamonds), as a function of initial monomer concentration.

conditions, M is field-independent and roughly proportional to ρ, the density (number of particles within the volume defined by r) of a given aggregate:

$$M \propto \rho \propto \frac{n}{r^3} \propto r^{df-3} \propto n^{1-\frac{3}{df}} \qquad (19)$$

Because V and D are independent of aggregation state, we can combine Eqs. (17)–(19) to obtain a set of proportionalities:

$$1/T2_{SPIO} \propto \rho^2 r^2 \propto r^{2df-4} \propto n^{2-\frac{4}{df}} \qquad (20)$$

Since at (typical) low SPIO volume fractions, $1/T2_{SPIO}$ is approximately equal to R2 times the particle concentration [cf. Eq. (14)], Eq. (20) predicts an increase in T2 relaxivity with increasing aggregate size when the fractal dimension is greater than 2. In the limiting case where aggregates are composed of fully packed spherical particles (df=3) the proportionality reduces to an r^2 dependence.

We simulated fractal aggregates with df=2.2, which is on the high end of the reaction-limited aggregation regime. This choice of df is somewhat arbitrary, and one would expect the fractal dimension to vary considerably depending on the details of particle geometry and functionalization. Although variation of df within the typical range would have a large effect on predicted relaxivity, our simulations demonstrated that it had a negligible effect on kinetics (data not shown). For aggregates with df=2.2, relation (20) predicts a relaxivity proportional to

$n^{2/11}$. In order to characterize the relaxivity of a given population of aggregates, we therefore calculated the mass average of $n^{2/11}$ and scaled it by the known single-particle relaxivity.

Fig. 4A shows the temporal evolution of relative relaxivity (normalized by the unaggregated particle relaxivity) and corresponding percent change in MRI signal intensity during the SPIO aggregation and disaggregation time courses shown in Fig. 3A. Signal intensity was calculated by assuming a baseline T2 for the medium of 100 ms and setting the TE to the T2 observed in the presence of nonaggregated SPIOs. Fig. 4B shows the predicted apparent time constant (T_{obs}, defined as above) of the change in MRI signal intensity, along with the maximal steady-state signal change, as a function of particle concentration. These results suggest that single-second temporal resolution may be possible for aggregation sensors with particle concentrations in the 20- to 100-nM range, but that lower SPIO concentrations will lead to considerably slower response rates. From a practical standpoint, it is also useful to know how long it takes the aggregation-induced signal change to reach a minimal detection threshold. We defined $T_{5\%}$ to be the time it takes to obtain a 5% change in signal, during aggregation of initially fully disaggregated particles. Fig. 4B shows that at high concentrations, $T_{5\%}$ is predicted to be of order 0.1 s, but that at lower concentrations, where 5% is close to the maximal signal change, $T_{5\%}$ is close to 100 s and actually longer than T_{obs}.

3.3. Time-resolved imaging with CEST agents

3.3.1. Temporal resolution of CEST-based imaging

The CEST effect [19] has recently been explored as a basis for MRI contrast agents because of its potential independence of paramagnetic metal complexes and possible advantages in sensitivity compared with some T1 contrast agents. CEST contrast enhancement is achieved by selectively saturating the proton magnetization of a small pool of labile protons associated with a CEST agent; these protons exchange with bulk solvent, producing a decrease in the bulk magnetization that gives rise to the detected MRI signal. CEST techniques have been applied to produce contrast changes in vitro, using a variety of agents including paramagnetic lanthanide complexes (PARACEST agents) [51]. CEST contrast changes have also been created in vivo using saturation of amide protons of endogenous proteins or exogenous species [52,53]. With CEST-based sensors, the efficiency of saturation transfer from the agent depends on select features of the agent's chemical environment, giving rise to modulations in detected MRI intensity that could, in principle, be followed in a dynamic imaging experiment.

In CEST MRI, saturation transfer to longitudinal bulk magnetization takes place during a presaturation period TP, after which RF excitation is delivered and any CEST-related changes in bulk magnetization are measured with a standard readout module (GRE, SE, EPI, etc.). Usually, TP is set to
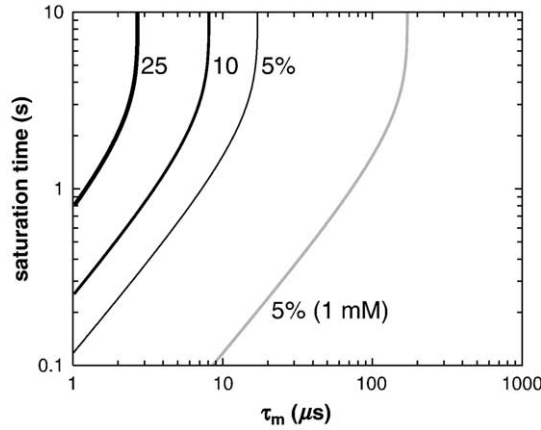
Fig. 5. Computed signal changes in dynamic MRI with CEST agents. Signal changes were calculated using Eq. (22) in the text, by considering the difference between signal in the absence and presence of chemical exchange, assuming complete saturation of the CEST pool ($\alpha = 1$) over a variable saturation period TP. Black contours show 5%, 10% and 25% signal change levels estimated for 100-μM CEST agent. Signal change contours for 1-mM agent are approximately parallel to these (contour for 5% change shown in gray), with <5% signal change observed at all TP values for low τ_m. A T1$_w$ of 1.0 s was assumed.

be almost as long as TR, in order to maximize CEST contrast for the given repetition rate. Observed CEST-dependent magnetization is influenced by the inherent spin-lattice relaxation rate of bulk water protons (1/T1$_w$), by the time constant (τ_m) for chemical exchange between CEST and bulk proton pools during the presaturation time, and by the efficiency and dynamics of the saturation itself. With a smart CEST contrast agent, τ_m and the saturation efficiency could depend on the configuration of the agent and would become time-dependent variables.

Analytical expressions for CEST-dependent MRI signal changes can be obtained under various simplifying assumptions [21,24]. A reasonable assumption is that the magnetization of the CEST pool reaches a steady state very rapidly during saturation (i.e., much faster than TP). A further approximation is that RF irradiation of the CEST pool does not directly saturate the bulk proton pool — this is true when the RF offset ($\Delta\omega$) between the bulk water frequency (ω_1) and CEST pool frequency satisfies: $\Delta\omega/\omega_1 \gg 1$. If these two conditions are met, and the steady-state partially saturated magnetization of the CEST proton pool is given by $(1-\alpha)M_{0s}$ (with M_{0s} being the equilibrium magnetization of the saturated CEST pool and α the fractional saturation of this pool), the following differential equation describes the evolution of bulk proton magnetization during TP:

$$\frac{dM_{zw}(t)}{dt} = \frac{(M_{0w} - M_{zw})}{T1_w} - \alpha\frac{M_{zw}}{\tau_w} \qquad (21)$$

$\tau_w = 111\tau_m/c$, where c is the concentration of exchange sites on the CEST agent and given a bulk proton concentration of 111 M. Assuming perfect RF flip angles (see T1 discussion above) and ideal CEST weighting

(TE<T2<TR~TP), a formula for relative signal observed in a serial imaging experiment can be obtained by integrating Eq. (21) over TP, with the initial condition that bulk magnetization is transverse ($M_{zw}=0$) before saturation begins:

$$I \propto \frac{\tau_w}{\tau_w + \alpha T1_w} - \frac{\tau_w}{\tau_w + \alpha T1_w}\exp\left\{-\frac{\tau_w + \alpha T1_w}{\tau_w T1_w}TP\right\} \qquad (22)$$

If a CEST-based MRI sensor was being used, terms in Eq. (22) would be replaced with integrals over TP, similar to Eqs. (10) and (13) (omitted here for notational simplicity). Because CEST contrast develops during the entire saturation period, the temporal resolution of a CEST experiment cannot exceed 1/TP. In analogy to the role of TR in T1-weighted molecular imaging, the requirement that TP be long enough to obtain sufficient CNR therefore sets a practical limit on the repetition time for MRI time series using CEST-based sensors.

Fig. 5 shows a contour plot of ideal CEST signal changes as a function of TP and τ_m, assuming a CEST agent is "turned on and off" with each image acquisition. The plot was calculated using Eq. (22) and overestimates signal change for cases where the RF offset ($\Delta\omega$) between the bulk water frequency (ω_1) and the saturated pool fails to satisfy $\Delta\omega/\omega_1 \gg 1$, when $\Delta\omega$ and the proton exchange time fail to obey $\tau_m\Delta\omega \gg 1$, or when $\alpha<1$ (as often expected under practical saturation powers). For any given noise level, the signal changes reported in the figure suggest realistic limitations on scan rate. The well-known dependence of the CEST effect on τ_m translates into faster possible time resolution for agents where saturation transfer changes occur around smaller τ_m values. The plot extends to τ_m's less than 10 μs, which have been reported for exchanging sites on some lanthanide complexes; at field strengths below 10 T, however, application of these complexes is likely to be compromised by the requirements on $\tau_m\Delta\omega$. As with T1-weighted imaging, the use of nonideal flip angles could degrade the temporal resolution below the CNR-dependent limit, by compromising the independence of each MRI acquisition. Temporal resolution could also be degraded if the CEST pool magnetization were not maintained near its steady-state value at all times, but we found no evidence of this in magnetization evolution simulations covering a broad range of conditions.

3.3.2. Response rates of CEST-based sensors

CEST agents have been used as MRI sensors for pH, lactate and glucose [9,10,15,20,53]. In all cases, the response rates of the sensors are likely to be extremely fast compared with the demands of the imaging method itself. CEST-based pH sensing is simplest to appreciate, given the well-known dependence of proton exchange rates on pH. Amide protons of endogenous proteins, and of two synthetic lanthanide complexes, have been used for pH-sensitive CEST [9,52,53]. Amide τ_m ranges from roughly 10^{-3} s^{-1} at pH 3 to 10^3 s^{-1} above pH 9 [54], creating a change in
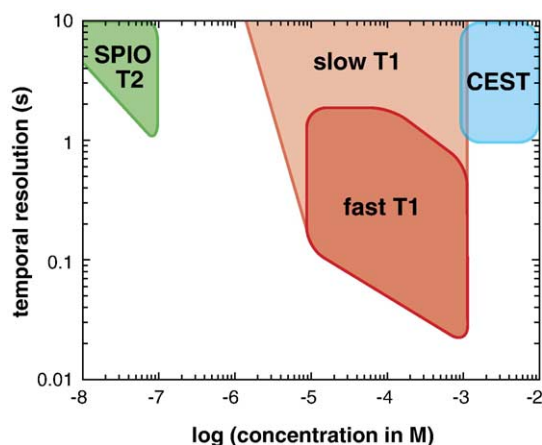
Fig. 6. Schematic comparison of temporal resolutions for three classes of molecular imaging agent. Colored regions approximate combinations of temporal resolution and contrast agent concentration that would lead to acceptable signal changes (>5%) with T1-weighted (red), T2-weighted (green) and CEST (blue) imaging. T1 agents are subdivided into "fast" agents (saturated red), for which imaging requirements limit the attainable temporal resolution, and "slow" agents (light red), for which properties of the agents themselves are limiting. See text for further discussion.

saturation transfer efficiency. The response rates to pH are likely to be extremely fast, although they have not been measured directly on the contrast agents. Rate constants for proton association reactions in general are thought to be on the order of 10^{10} to 10^{11} M^{-1} s^{-1} [55]. Base-catalyzed exchange is most common in the physiological pH range (pH 5–8) [52]; under base catalysis, the association and dissociation rate constants for glycine amide proton exchange (similar to the CEST pH sensor DOTAM-Gly) are roughly 1.4×10^{11} and 8×10^5 s^{-1}, respectively [55]. Given these rates, it is likely that the response of CEST agents to pH changes takes place within a few microseconds. This timescale is negligible compared with the duration of presaturation pulses used to measure pH changes from agent concentrations even over 10 mM.

A related mechanism underlies low affinity glucose detection by a complex synthesized by Zhang et al. [20]. The unliganded form of the sensor functions efficiently as a CEST agent, due to exchange of water molecules at a free europium coordination site. In the presence of glucose (K_d=2.6 mM), the exchange site is partially blocked (cf. Fig. 1A), leading to a noticeable reduction in CEST efficiency when saturation is delivered at a −30 ppm RF offset. A somewhat different mechanism allows CEST-based lactate sensing by an agent called MBDO3AM [15]. In its free state, this lanthanide adduct contains six amide protons, all of which overlap to give rise to a high field-shifted proton resonance peak at −28.5 ppm. When lactate is added at relatively high concentrations (the dissociation constant is over 100 μM), the degenerate resonance is resolved into discrete peaks in a lower field frequency range, −14 to −20 ppm. If saturation is selectively directed either at the free MBDO3AM amide

peaks, or at the complexed-form amides, a change in CEST saturation efficiency results from binding of the lactate to the contrast agent. With neither the glucose nor the lactate sensor being a kinetic parameter describing the metabolite/ sensor binding interaction known, but by analogy with other bimolecular binding pairs, the association rates are likely to be well over 10^5 M^{-1} s^{-1}, implying that the dissociation rates are at least 10 s^{-1}. Even given these conservative estimates, the kinetics of intermolecular interactions that underlie CEST-based lactate and glucose sensing are still significantly faster than the timescale used to build up CEST contrast, which was on the order of several seconds in these studies.

3.4. Comparison of dynamic molecular MRI methods

Fig. 6 presents a comparison of temporal resolutions for dynamic imaging approaches using smart T1 contrast agents, SPIO aggregation-based T2 sensors and CEST agents. For each of the three groups of molecular imaging agents we considered, a colored area denotes approximate conditions under which acceptable signal changes may be achieved, assuming realistic MRI acquisition conditions. This representation is a guideline only; it is by necessity highly reductionist, because the full range of relaxivities and interconnected trade-offs between CNR, repetition rate, spatial resolution, partial volume effects and signal averaging are impossible to address simultaneously in graphical form. Roughly speaking, we assume that a 5% signal change is sufficient for detection of an agent's response in a time-resolved experiment. This requirement is lower than the standard generally required in contrast agent-enhanced anatomical (static) imaging, but reflects the important possibility, specific to dynamic imaging, of performing statistically rigorous within-subject comparisons to recognize small image intensity fluctuations. In human fMRI, the dominant form of time-resolved MRI today, signal changes lower than 1% are often robustly detected at the single-voxel level.

The "fast" T1 agent area in Fig. 6 (saturated red) was estimated assuming GRE imaging with $\pi/2$ excitation pulses, and a sensor with relaxivity changes on the millisecond or faster timescale, from 5 to 10 mM^{-1} s^{-1}. The region is bounded at the right by concentration levels at which toxicity and T2 effects may interfere with applications; at low concentrations, signal changes are likely to be below the detection limit. In principle, TRs close to 10 ms could be used to obtain even higher temporal resolution than shown, but this would result in severe attenuation of the overall signal and under typical imaging conditions would be impractical. Very short TRs would also be incompatible with EPI volume acquisition. The "slow" T1 area in light red refers to T1 agents like the Gal80-binding agent and the β-galactosidase substrate discussed above, for which the molecular rate of response is the limiting factor on potential temporal resolution. The relaxivity changes produced by these sensors are on the same order of

magnitude as the "fast" agents, but signal averaging becomes a possibility when time resolution is no longer limiting, so it is likely that somewhat lower concentrations could be used.

The aggregation-based SPIO agents are represented by the green-shaded area. For these agents, the temporal resolution in T2-weighted imaging is also limited by the sensors' rates of response, rather than by the imaging itself. The region plotted in Fig. 6 is estimated based on the theoretical analysis we have performed here; our modeling was consistent with data from the literature, but covered a wider variety of conditions than has yet been experimentally explored. The response times of aggregation-based sensors are predicted to vary approximately linearly from about 100 s at 1 nM SPIO concentration to 1 s at 0.1 μM, for particles with ~50 attached proteins; if the functionalization level is lowered, the rates would be decreased. At SPIO concentrations into the micromolar range, the aggregation effect would be yet faster, but concentrations significantly above 0.1 μM (10 mg/L Fe, assuming 2000 iron atoms per particle) would begin to attenuate the MRI signal too severely and would be inconsistent with physical echo times.

The blue area in Fig. 6 denotes conditions under which dynamic MRI with smart CEST agents could be performed. As our earlier discussion emphasized, the temporal resolutions and concentrations compatible with use of existing CEST-based sensors are completely constrained by the physical requirements of performing imaging with acceptable signal changes. To estimate the region in Fig. 6, we performed pulse sequence and magnetization simulations for a 300-μs τ_m CEST agent, under a range of repetition rates and concentrations, with TP~TR. Signal changes between exchanging ("on") and nonexchanging ("off") conditions were greater than 5% for concentrations above 1 mM and for 1- to 10-s saturation times. If agents with lower τ_m were used at very high field, it is likely that lower saturation times or concentrations could be used.

A conclusion from this comparison is that the fastest MRI molecular imaging temporal resolution (~100 ms) is likely to be obtained with T1 agents, while the lowest concentrations (and greatest signal changes) may be reached with SPIO aggregation sensors. Several caveats apply: First, most of our arguments have relied on simulations or calculations performed under idealizing assumptions; some of the findings (especially the aggregation simulations) await empirical validation and may incompletely account for realistic experimental conditions. Second, the discussion has focused on time dependence largely to the exclusion of other factors related to the contrast agents. In an actual dynamic MRI experiment, some agents with inferior "theoretical" time resolution may in fact be preferable for unrelated reasons. Third and last, we have not attempted a comprehensive discussion of all existing or putative smart contrast agents and mechanisms — the specific agents we have addressed were chosen because they are representative or of particular interest.

The guide we present in Fig. 6, and the more detailed analyses of the previous sections, gives an overview of considerations important to dynamic molecular imaging experiments. Although few such experiments have been reported to date, time-resolved molecular imaging of biologically significant targets (particularly in neuroscience and developmental biology) is clearly an urgent direction in MRI methods development. Quantitative description of contrast agent properties will help direct both the selection of viable experimental strategies and the design of new smart contrast agents with improved characteristics. Our discussion suggests that high CNR is the most important requirement for optimizing temporal resolution with T1 agents, where the sensitivity of the MRI methods currently limits acquisition rates. The development of T2 SPIO agents with enhanced kinetic properties is also clearly recommended, given the low concentrations at which these agents can be used; improved SPIO-based sensors could be produced by maximizing nanoparticle functionalization levels, or by loosely tethering particles to one another in order to speed aggregation.

Acknowledgments

References

[1] Schmitt F, Stehling MK, Turner R. Echo-planar imaging: theory, technique, and application. Berlin: Springer; 1998.

[2] Meade TJ, Taylor AK, Bull SR. New magnetic resonance contrast agents as biochemical reporters. Curr Opin Neurobiol 2003;13:597–602.

[3] Jasanoff A. Functional MRI using molecular imaging agents. Trends Neurosci 2005;28:120–6.

[4] Kayyem JF, Kumar RM, Fraser SE, Meade TJ. Receptor-targeted co-transport of DNA and magnetic resonance contrast agents. Chem Biol 1995;2:615–20.

[5] Louie AY, Huber MM, Ahrens ET, Rothbacher U, Moats R, Jacobs RE, et al. In vivo visualization of gene expression using magnetic resonance imaging [In Process Citation]. Nat Biotechnol 2000;18:321–5.

[6] Weissleder R, Moore A, Mahmood U, Bhorade R, Benveniste H, Chiocca EA, et al. In vivo magnetic resonance imaging of transgene expression. Nat Med 2000;6:351–5.

[7] Zhao M, Beauregard DA, Loizou L, Davletov B, Brindle KM. Non-invasive detection of apoptosis using magnetic resonance imaging and a targeted contrast agent. Nat Med 2001;7:1241–4.

[8] Lowe MP, Parker D, Reany O, Aime S, Botta M, Castellano G, et al. pH-Dependent modulation of relaxivity and luminescence in macrocyclic gadolinium and europium complexes based on reversible

intramolecular sulfonamide ligation. J Am Chem Soc 2001;123: 7601–9.

[9] Aime S, Barge A, Delli Castelli D, Fedeli F, Mortillaro A, Nielsen FU, et al. Paramagnetic lanthanide(III) complexes as pH-sensitive chemical exchange saturation transfer (CEST) contrast agents for MRI applications. Magn Reson Med 2002;47:639–48.

[10] Zhou J, Lal B, Wilson DA, Laterra J, van Zijl PC. Amide proton transfer (APT) contrast for imaging of brain tumors. Magn Reson Med 2003;50:1120–6.

[11] Aime S, Botta M, Gianolio E, Terreno E. A p(O$_2$)-responsive MRI contrast agent based on the redox switch of manganese (II/III)–porphyrin complexes. Angew Chem Int Ed Engl 2000;39: 747–50.

[12] Sun PZ, Schoening ZB, Jasanoff A. In vivo oxygen detection using exogenous hemoglobin as a contrast agent in magnetic resonance microscopy. Magn Reson Med 2003;49:609–14.

[13] Li W, Fraser SE, Meade TJ. A calcium-sensitive magnetic resonance imaging contrast agent. J Am Chem Soc 1999;121:1413–4.

[14] Hanaoka K, Kikuchi K, Urano Y, Narazaki M, Yokawa T, Sakamoto S, et al. Design and synthesis of a novel magnetic resonance imaging contrast agent for selective sensing of zinc ion. Chem Biol 2002;9:1027–32.

[15] Aime S, Delli Castelli D, Fedeli F, Terreno E. A paramagnetic MRI-CEST agent responsive to lactate concentration. J Am Chem Soc 2002;124:9364–5.

[16] Perez JM, Josephson L, O'Loughlin T, Hogemann D, Weissleder R. Magnetic relaxation switches capable of sensing molecular interactions. Nat Biotechnol 2002;20:816–20.

[17] Lauffer RB. Paramagnetic metal complexes as water proton relaxation agents for NMR imaging: theory and design. Chem Rev 1987;87: 901–27.

[18] Perez JM, Josephson L, Weissleder R. Use of magnetic nanoparticles as nanosensors to probe for molecular interactions. Chembiochem 2004;5:261–4.

[19] Ward KM, Aletras AH, Balaban RS. A new class of contrast agents for MRI based on proton chemical exchange dependent saturation transfer (CEST). J Magn Reson 2000;143:79–87.

[20] Zhang S, Trokowski R, Sherry AD. A paramagnetic CEST agent for imaging glucose by MRI. J Am Chem Soc 2003;125:15288–9.

[21] Zhou J, Wilson DA, Sun PZ, Klaus JA, Van Zijl PC. Quantitative description of proton exchange processes between water and endogenous and exogenous agents for WEX, CEST, and APT experiments. Magn Reson Med 2004;51:945–52.

[22] Ahrens ET, Rothbacher U, Jacobs RE, Fraser SE. A model for MRI contrast enhancement using T1 agents. Proc Natl Acad Sci U S A 1998;95:8443–8.

[23] Allen MJ, Meade TJ. Magnetic resonance contrast agents for medical and molecular imaging. Met Ions Biol Syst 2004;42:1–38.

[24] Woessner DE, Zhang S, Merritt ME, Sherry AD. Numerical solution of the Bloch equations provides insights into the optimum design of PARACEST agents for MRI. Magn Reson Med 2005;53: 790–9.

[25] Dahnke H, Schaeffter T. Limits of detection of SPIO at 3.0 T using T2 relaxometry. Magn Reson Med 2005;53:1202–6.

[26] Odriozola G, Moncho-Jorda A, Schmitt A, Callejas-Fernandez J, Martinez-Garcia R, Hidalgo-Alvarez R. A probabilistic aggregation kernel for the computer-simulated transition from DLCA to RLCA. Europhys Lett 2001;53:797–803.

[27] Laurenzi IJ, Diamond SL. Kinetics of random aggregation–fragmentation processes with multiple components. Phys Rev E Stat Nonlinear Soft Matter Phys 2003;67:051103.

[28] Callaghan PT. Principles of nuclear magnetic resonance microscopy. Oxford (UK): Oxford University Press; 1993.

[29] Toth E, Helm L, Merbach AE. Relaxivity of gadolinium(III) complexes: theory and mechanism. In: Merbach AE, Toth E, editors. The chemistry of contrast agents in medical magnetic resonance imaging. New York: Wiley; 2001.

[30] Li WH, Parigi G, Fragai M, Luchinat C, Meade TJ. Mechanistic studies of a calcium-dependent MRI contrast agent. Inorg Chem 2002; 41:4018–24.

[31] McHugh JM, Kenyon JL. An Excel-based model of Ca^{2+} diffusion and fura 2 measurements in a spherical cell. Am J Physiol Cell Physiol 2004;286:C342–8.

[32] De Leon-Rodriguez LM, Ortiz A, Weiner AL, Zhang S, Kovacs Z, Kodadek T, et al. Magnetic resonance imaging detects a specific peptide-protein binding event. J Am Chem Soc 2002;124: 3514–5.

[33] Fersht AR. Enzyme structure and mechanism. New York: W.H. Freeman & Co.; 1985.

[34] Lauffenburger DA, Linderman JJ. Receptors: models for binding, trafficking, and signaling. New York: Oxford University Press; 1993.

[35] Ogawa S, Tank DW, Menon R, Ellermann JM, Kim SG, Merkle H, et al. Intrinsic signal changes accompanying sensory stimulation: functional brain mapping with magnetic resonance imaging. Proc Natl Acad Sci U S A 1992;89:5951–5.

[36] Chen YC, Mandeville JB, Nguyen TV, Talele A, Cavagna F, Jenkins BG. Improved mapping of pharmacologically induced neuronal activation using the IRON technique with superparamagnetic blood pool agents. J Magn Reson Imaging 2001;14:517–24.

[37] Bulte JW, Kraitchman DL. Iron oxide MR contrast agents for molecular and cellular imaging. NMR Biomed 2004;17:484–99.

[38] Bonnemain B. Superparamagnetic agents in magnetic resonance imaging: physicochemical characteristics and clinical applications. A review. J Drug Target 1998;6:167–74.

[39] Wang YX, Hussain SM, Krestin GP. Superparamagnetic iron oxide contrast agents: physicochemical characteristics and applications in MR imaging. Eur Radiol 2001;11:2319–31.

[40] Josephson L, Perez JM, Weissleder R. Magnetic nanosensors for the detection of oligonucleotide sequences. Angew Chem Int Ed Engl 2001;40:3204–6.

[41] Perez JM, O'Loughin T, Simeone FJ, Weissleder R, Josephson L. DNA-based magnetic nanoparticle assembly acts as a magnetic relaxation nanoswitch allowing screening of DNA-cleaving agents. J Am Chem Soc 2002;124:2856–7.

[42] Atanasijevic T, Fam PS, Jasanoff A. Protein-nanoparticle conjugates as dynamic calcium reporters for magnetic resonance imaging. 2005 [in preparation].

[43] Smoluchowski M. Versuch einer mathematischen Theorie der Koagulationskinetik kolloider Losungen. Z Phys Chem 1917;92: 129–68.

[44] Odriozola G, Schmitt A, Moncho-Jorda A, Callejas-Fernandez J, Martinez-Garcia R, Leone R, et al. Constant bond breakup probability model for reversible aggregation processes. Phys Rev E Stat Nonlinear Soft Matter Phys 2002;65(3 Pt 1):031405.

[45] Verkman AS. Solute and macromolecule diffusion in cellular aqueous compartments. Trends Biochem Sci 2002;27:27–33.

[46] Gillis P, Moiny F, Brooks RA. On T(2)-shortening by strongly magnetized spheres: a partial refocusing model. Magn Reson Med 2002;47:257–63.

[47] Roch A, Gossuin Y, Muller RN, Gillis P. Superparamagnetic colloid suspensions: water magnetic relaxation and clustering. J Magn Magn Mater 2005;293:532–9.

[48] Shen T, Weissleder R, Papisov M, Bogdanov Jr A, Brady TJ. Monocrystalline iron oxide nanocompounds (MION): physicochemical properties. Magn Reson Med 1993;29:599–604.

[49] Vicsek T. Fractal growth phenomena. Hackensack (NJ): World Scientific; 1992.

[50] Zhou CL, Zhao Y, Jao TC, Wu C, Winnik MA. Effect of concentration on the photoinduced aggregation of polymer nanoparticles. J Phys Chem B 2002;106:9514–21.

[51] Zhang S, Merritt M, Woessner DE, Lenkinski RE, Sherry AD. PARACEST agents: modulating MRI contrast via water proton exchange. Acc Chem Res 2003;36:783–90.

[52] Zhou J, Payen JF, Wilson DA, Traystman RJ, Van Zijl PC. Using the amide proton signals of intracellular proteins and peptides to detect pH effects in MRI. Nat Med 2003;9:1085–90.

[53] Raghunand N, Zhang S, Sherry AD, Gillies RJ. In vivo magnetic resonance imaging of tissue pH using a novel pH-sensitive contrast agent, GdDOTA-4AmP. Acad Radiol 2002;9(Suppl 2):S481–3.

[54] Zhang YZ, Paterson Y, Roder H. Rapid amide proton exchange rates in peptides and proteins measured by solvent quenching and two-dimensional NMR. Protein Sci 1995;4:804–14.

[55] Eigen M. Proton transfer, acid–base catalysis, and enzymatic hydrolysis: Part I. Elementary processes. Angew Chem Int Ed Engl 1964;3:1–19.